High Electron Mobility and Insights into Temperature-Dependent Scattering Mechanisms in InAsSb Nanowires

Jessica L. Boland,[†] Francesca Amaduzzi,[‡] Sabrina Sterzl,[†] Heidi Potts,[‡] Laura M Herz,[†] Anna Fontcuberta I Morral,[‡] and Michael B. Johnston[*,†]

[†]*Department of Physics, University of Oxford, Clarendon Laboratory, Parks Road, Oxford, OX1 3PU, United Kingdom*

[‡]*Laboratory of Semiconductor Materials, École Polytechnique Fédérale de Lausanne (EPFL), CH-1015 Lausanne, Switzerland*

E-mail: michael.johnston@physics.ox.ac.uk

Abstract

InAsSb nanowires are promising elements for thermoelectric devices, infrared photodetectors, high-speed transistors, as well as thermophotovoltaic cells. By changing the Sb alloy fraction the mid-infrared bandgap energy and thermal conductivity may be tuned for specific device applications. Using both terahertz and Raman non-contact probes, we show that Sb alloying increases the electron mobility in the nanowires by over a factor of 3 from InAs to $InAs_{0.65}Sb_{0.35}$. We also extract the temperature-dependent electron mobility via both terahertz and Raman spectroscopy and we report the highest electron mobilities for $InAs_{0.65}Sb_{0.35}$ nanowires to date, exceeding $16{,}000\,cm^2V^{-1}s^{-1}$ at 10 K.

Keywords

InAsSb nanowires, quasi-pure-phase, Raman spectroscopy, THz spectroscopy, enhanced photoconductivity lifetimes, enhanced mobility

Introduction

Semiconductor nanowires are prime candidates for the development of nanoscale optoelectronic and thermoelectric devices. Their unique one-dimensional geometry has opened up a new playing field for the growth of complex radial and axial nanoscale heterostructures that can be directly integrated with silicon.[1] To date, many nanowire-based optoelectronic devices have already been demonstrated, such as nanowire solar cells,[2–6] field-effect transistors,[7–11] nanowire lasers,[12–16] and terahertz detectors,[17–20] to name a few.

Ternary alloying of indium-based III–V nanowires is of great interest, as indium-based nanowires have been found to possess many desirable properties for high speed optoelectronic and spintronic devices, including very high electron mobilities, high spin-orbit coupling and large g-factors.[21–27] In particular by adjusting the alloy fraction x of the ternary semicon-

ductor $InAs_{1-x}Sb_x$ it is possible to tune the material's absorption and emission spectra throughout the mid-infrared spectrum, from 0.35 eV for $x = 0$ to $0.1, \text{eV}$ for $x = 0.65$.[28] Indeed, $InAs_{0.35}Sb_{0.65}$ has the lowest bandgap of any III-V semiconductor.[29] The tunabilty of bandgap offered by $InAs_{1-x}Sb_x$ allows infrared photodetectors, light emitting diodes and lasers[30] to be optimised for specific applications, and is useful when designing thermophotovoltaic cells for heat sources of a particular temperature.

$InAs_{1-x}Sb_x$ nanowires also show promise for thermoelectric applications, which require materials with high electron mobilty but low thermal conductivity. Bulk InAs and InSb have already been benchmarked as ideal thermoelectric materials, owing to their narrow mid-infrared bandgaps, high intrinsic carrier densities and low thermal conductivities of $0.27\,\text{Wcm}^{-1}\text{K}^{-1}$ and $0.18\,\text{Wcm}^{-1}\text{K}^{-1}$ respectively.[31] Investigations into thermal and electronic properties of nanowires based on these materials have been carried out, with initial studies displaying a reduction in thermal conductivity compared to bulk crystals and high electron mobilities on the order of $\sim 6000\,\text{cm}^2\text{V}^{-1}\text{s}^{-1}$ at 300 K and $\sim 25,000\,\text{cm}^2\text{V}^{-1}\text{s}^{-1}$ at 4.2K.[25,32–37] However, despite their promise for numerous device applications, studies into the optoelectronic properties of ternary $InAs_{1-x}Sb_x$ nanowire structures remain in their infancy.

So far, previous studies on ternary antimonide III-V nanowires have focused on structural changes within the nanowire, which occur even at minute doping concentrations.[28,38,39] As zinc-blende stacking in Sb crystals is usually favoured owing to the small ionicity of the bond, III-V antimonide nanowires have been shown to exhibit predominately-pure zinc-blende nanowire structures. Specifically, such crystal perfection has been observed in $InAs_{1-x}Sb_x$ nanowires, with Zhuang et al. noting a quasi-pure zinc-blende structure for MBE-grown $InAs_{1-x}Sb_x$ nanowires at 10% Sb concentration[39] with a low stacking fault density of 50 defects μm^{-1}, while Farrell et al. demonstrated predominantly zinc-blende MOCVD-grown InAsSb nanowires at 6% Sb concentration, with a stacking fault density of 70 defects μm^{-1}.[40] However, although both of these works demonstrated a significant reduction in stacking fault density with increasing Sb concentration, the density of twin planes within the nanowire remained high

at 269 defects μm^{-1} and 350 defects μm^{-1} respectively. By employing catalyst-free growth, Potts et al. have recently demonstrated that the twin defect density can also be reduced by Sb incorporation, with the number of interfaces (stacking faults, ZB/WZ polytypism and rotational twins) amounting to only a few defects per micron for Sb contents higher than 20%.[41] Accompanying this high crystal quality, III-V antimonide nanowires have also been shown to exhibit an increase in carrier mobility with increasing Sb content.[41,42] This mobility enhancement is particularly promising, as alloy disorder scattering is expected to increase due to Sb incorporation and degrade the electron mobility. Therefore, in order to further understand the effect of Sb alloying on the electron mobility and carrier transport in these $InAs_{1-x}Sb_x$ nanowires, accurate characterisation of the electronic properties as a function of Sb content is essential.

In this work, we utilize and compare two non-contact, non-invasive techniques – optical-pump terahertz-probe (OPTP) spectroscopy and Raman spectroscopy – to extract the electron mobilities, photoconductivity lifetimes, and carrier concentrations in $InAs_{1-x}Sb_x$ nanowires with varying Sb contents of x =0, 0.16, 0.21, and 0.35. We also extract the mid-infrared bandgap of $InAs_{1-x}Sb_x$ nanowires via photoluminescence (PL) spectroscopy, demonstrating optical bandgap engineering throughout the infrared spectrum. From terahertz measurements, we demonstrate an increase in photoconductivity lifetime by over a factor of 3 with increasing Sb concentration, with a photoconductivity lifetime of 486 ± 30 ps for the $InAs_{0.65}Sb_{0.35}$ nanowires compared to 130 ± 40 ps for an InAs nanowire reference sample. The enhancement is attributed to the reduction in crystal defect density induced by Sb incorporation, which suppresses carrier trapping at nanowire defects. For the first time, we compare two non-contact techniques, terahertz and Raman spectroscopy, and extract both the free carrier concentration and electron mobility within the nanowires as a function of temperature. We exhibit high room-temperature electron mobilities of $7740 \pm 650\ cm^2V^{-1}s^{-1}$ (THz) and $8300 \pm 913\ cm^2V^{-1}s^{-1}$ (Raman) for the $InAs_{0.65}Sb_{0.35}$ nanowires, over a factor of 3 higher than for the InAs nanowires at $2710 \pm 320\ cm^2V^{-1}s^{-1}$ (THz) and $3300 \pm 1900\ cm^2V^{-1}s^{-1}$ (Raman).

We find that at low temperatures, where defect-density scattering dominates, a reduction in the momentum scattering of electrons can be seen with increased Sb concentration, with electron mobilities reaching $16000\pm210\,\mathrm{cm^2V^{-1}s^{-1}}$ (THz) and $17500\pm2450\,\mathrm{cm^2V^{-1}s^{-1}}$ (Raman) for the $InAs_{0.65}Sb_{0.35}$ nanowires compared to $6160\pm360\,\mathrm{cm^2V^{-1}s^{-1}}$ (THz) and $5100\pm2200\,\mathrm{cm^2V^{-1}s^{-1}}$ (Rama for the InAs reference nanowires at $\sim$10 K. This observed reduction of momentum scattering suggests that Sb alloying improves the mobility of $InAs_{1-x}Sb_x$ nanowires not only due to the reduced effective electron mass at higher Sb contents but also as a result of the improved crystal quality, which reduces defect scattering within the nanowire.

InAs and $InAs_{1-x}Sb_x$ nanowires were grown vertically and self-catalysed on GaAs(111)B substrates via molecular beam epitaxy (MBE).[41] To obtain a maximum yield of $InAs_{1-x}Sb_x$ with minimal variation in nanowire diameter and length, the growth substrates were coated with a thin layer of silicon oxide of thickness 4.5 mm and an optimum growth temperature of 520°C applied. The antimony flux was increased during growth to produce $InAs_{1-x}Sb_x$ nanowires of varying Sb alloy fractions of: $x = 0$, 0.11, 0.16, 0.21, 0.35.[41] The elemental composition of the nanowires was verified via energy dispersive x-ray spectroscopy in an FEI Tecnai OSIRIS microscope at 200kV. The nanowires possessed diameters of 71 ± 6 nm, 79 ± 5 nm, 74 ± 5 nm, 82 ± 7 nm and 85 ± 6 nm respectively and were all approximately 2 μm in length. More details about nanowire growth can be found in the Supporting Information.[41] The nanowire samples were kept on their growth substrate for Raman and PL spectroscopy, however, for terahertz measurements, they were transferred to z-cut quartz substrates.

First, to investigate the effect of Sb incorporation on the optical properties of $InAs_{1-x}Sb_x$ nanowires, we utilise PL spectroscopy to extract the bandgap energy, E_{gap}, at varying Sb concentrations. Figure 1(a) shows the PL spectra measured at a temperature of 6 K as a function of emission energy for a bulk InAs wafer and $InAs_{1-x}Sb_x$ nanowires with Sb concentrations of 11%, 16% and 35%. Due to a low nanowire density, a PL signal could not be obtained from the $InAs_{0.79}Sb_{0.21}$ nanowires. The nanowires were excited with a continuous wave laser at a centre wavelength of 532 nm, at an average photoexcitation power of

200 mW/cm^2 and PL spectra measured using an FTIR spectrometer and a mercury cadmium telluride detector at a resolution of 50 cm^{-1}. In-depth details of the experimental setup can be found in the Supporting Information. From the PL spectra, a clear red-shift in the PL peak position and thereby bandgap energy can be observed for the $InAs_{1-x}Sb_x$ nanowires, as Sb content is increased. To facilitate the extraction of the bandgap energy, a Gaussian was fitted to each individual PL spectra and the peak energy plotted as a function of Sb content in Figure 1(b). The bandgap energy of the $InAs_{1-x}Sb_x$ nanowires is clearly reduced as an effect of Sb incorporation, with the lowest bandgap energy at 35% Sb content determined to be 230 meV compared to 410 meV for bulk InAs.

The bandgap of alloyed semiconductor such as $InAs_{1-x}Sb_x$ may be fitted as a quadratic function of the Sb alloy fraction x as follows:

$$E_{\text{gap}} = xE_{\text{InSb}} + (1-x)E_{\text{InAs}} - Cx(1-x), \tag{1}$$

where, E_{InSb} and E_{InAs} are the bandgap energies for InSb and InAs respectively, and C is the bowing parameter. The solid curve in Figure 1(b) shows Equation 1 calculated by setting the bandgaps of InSb and InAs to their bulk values of $E_{\text{InSb}} = 235$ meV and $E_{\text{InAs}} = 415$ meV at 6 K and setting the bowing parameter to $C = 662$ meV.[40,43] This value has previously been determined experimentally for similar InAsSb nanowire structures and coincides well with the established value of bulk InAsSb at 700 meV.[44] A good agreement is found between the function and the bandgap energies extracted from the measured PL spectra. It is important to note that slight deviations of the measured bandgap energy from the established bulk values are expected due to the non-uniform distribution of the antimony content in the radial direction of the nanowire[45] and variations in crystal structure, as bandgap energies differ between wurtzite and zinc-blende structures of the same material. However, the PL measurements suggest that for these MBE-grown $InAs_{1-x}Sb_x$ nanowires, the deviation is minimal, allowing for accurate bandgap engineering via Sb incorporation in InAs

nanowires.[46] The low bandgap energy of $\sim 230\,\text{meV}$ for the $InAs_{0.65}Sb_{0.35}$ nanowires renders them ideal candidates for thermoelectric and thermophotovoltaic applications.

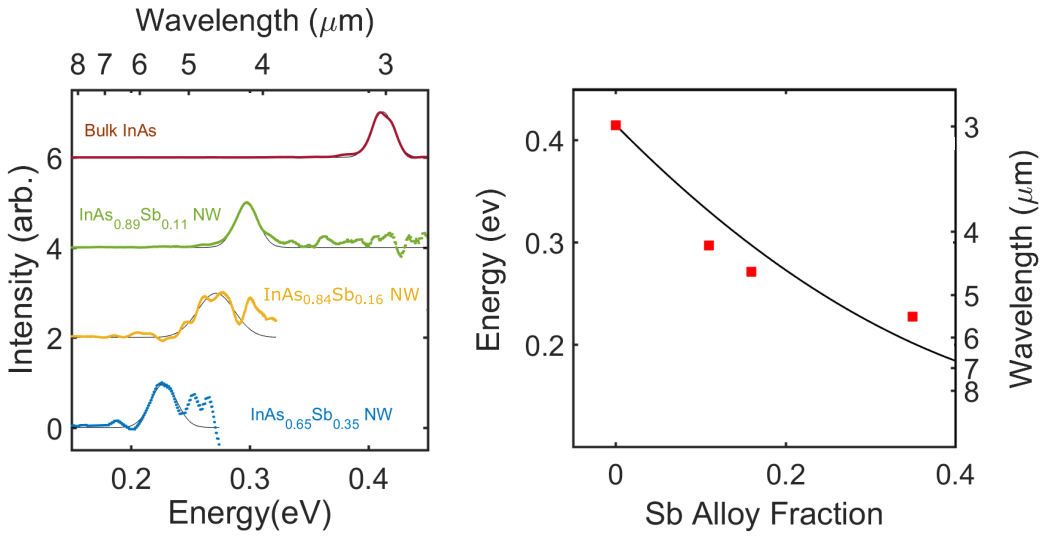

Figure 1: (a) Photoluminescence spectra of bulk InAs (black) and $InAs_{1-x}Sb_x$ nanowires with varying Sb contents of 11%, 16% and 35% (red, blue, green) as a function of emission energy with Gaussian fits shown as solid black lines. All samples were held at a temperature of 6 K during the measurements. (b) Extracted bandgap energies as a function of Sb content. Equation 1 with $C = 662\,\text{meV}$, $E_{\text{InSb}} = 235\,\text{meV}$ and $E_{\text{InAs}} = 415\,\text{meV}$ is plotted as a solid black line.

Following on from these promising results, we employ two non-contact techniques – OPTP and Raman spectroscopy – to further examine the optoelectronic properties of these $InAs_{1-x}Sb_x$ nanowires. We investigate the effect of Sb alloying on two key transport properties that can hinder device performance: photoconductivity lifetime and electron mobility. First, we utilise OPTP spectroscopy to investigate the effect of Sb incorporation on the nanowire photoconductivity lifetime. The nanowires were photoexcited by a near infrared laser with pulses of 35 fs duration, at a centre wavelength of 800 nm (E_{photon} =1.55 eV) for a range of fluences between 0.46 and $244\,\mu\,\text{J}\,\text{cm}^{-2}$. This photoexcitation generates electron-hole pairs uniformly across the whole nanowire and induces a change, ΔE, in the electric field transmission of the THz probe pulse, E. The ratio of this change to the THz probe transmission, $|\frac{\Delta E}{E}|$, is proportional to the photoinduced conductivity, $\Delta\sigma$, of the nanowires and thereby the change in free carrier concentration.[47] This photoinduced conductivity can

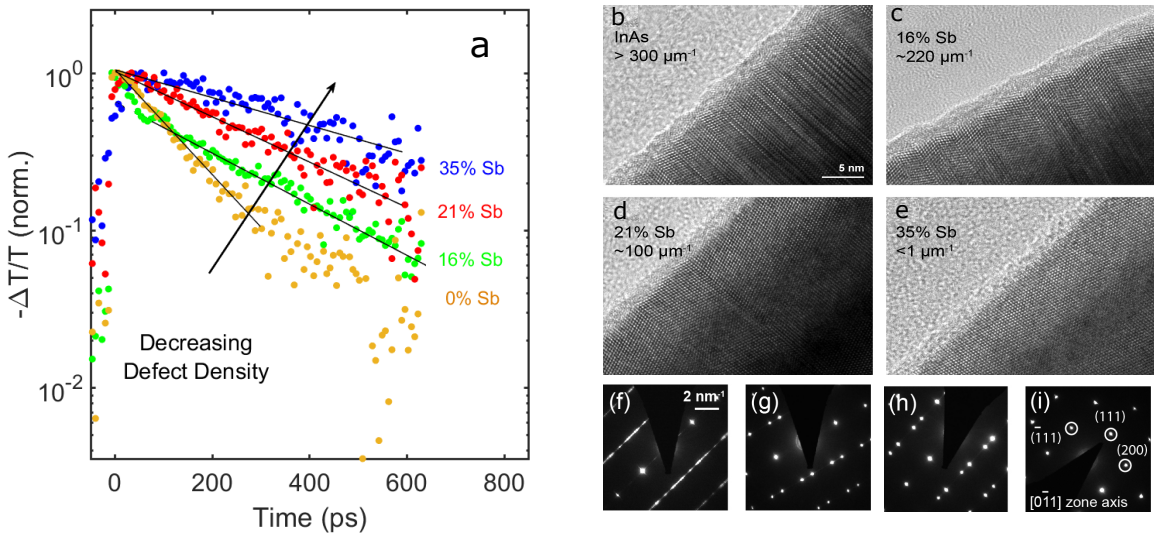

Figure 2: a) Terahertz measurements of the normalised photoconductivity decay taken at a fluence of 190 μ J cm^{-2} as a function of time after photoexcitation for the InAs reference nanowires (orange) $InAs_{1-x}Sb_x$ nanowires with Sb concentrations of 16%, (green), 21% (red) and 35% (blue). Monoexponential fits to the decay curves are depicted by solid black lines. TEM images for (b) InAs nanowires and $InAs_{1-x}Sb_x$ nanowires with Sb concentrations of (c) 16%, (d) 21% and (e) 35%. TEM Diffraction pattern images for the (f) InAs nanowires and $InAs_{1-x}Sb_x$ nanowires with Sb concentrations of (g) 16%, (h) 21% and (i) 35%, showing decrease in defect density with increasing Sb content.

then be measured as a function of time delay between the photoexcitation beam and the THz beam, thereby enabling the electrical conductivity to be extracted as a function of time after photoexcitation.

Figure 2(a) shows the time-resolved photoconductivity as a function of time after photoexcitation for the InAs nanowire reference sample and $InAs_{1-x}Sb_x$ nanowires with varying Sb content at a photoexcitation fluence of $190\,\mu\,J\,cm^{-2}$. For all samples, the photoconductivity shows a rapid rise within the first 10 ps after photoexcitation followed by a slower monoexponential decay. As excitonic behaviour is not expected to dominate in InAs or $InAs_{1-x}Sb_x$ nanowires at room temperature, the monoexponentional behaviour is attributed to monomolecular recombination dominating, due to Shockley-Read-Hall recombination and carrier trapping at the surface and at defects within the nanowire. By globally fitting a monoexponential to the photoconductivity decays taken at different fluences, we determined the recombination rates and thereby photoconductivity lifetimes with high accuracy for all nanowire samples. From comparison of the photoconductivity decays in Figure 2, it can clearly be observed that the photoconductivity lifetime increases with increasing Sb content. The photoconductivity lifetime for the InAs nanowires was found to be 130 ± 40 ps, coinciding with previous literature values for InAs nanowires.[25] This short lifetime is attributed to the high surface recombination velocity for InAs nanowires,[25] which causes photoexcited electrons to be rapidly trapped at the nanowire surface. For the $InAs_{1-x}Sb_x$ nanowires, the photoconductivity lifetimes were extracted to be: 285±42 ps, 300±52 ps and 486±26 ps for 16%, 21% and 35% Sb content, respectively. It is important to note that the increase in nanowire diameter for higher Sb contents would have a small contribution to the increase in photoconductivity lifetime, as surface recombination would be reduced due to the lower surface-to-volume ratio. However, the nanowire diameters for all samples are comparable, with only a 9 nm difference between the smallest and largest diameter, so this effect is not expected to be the dominant contribution for prolonging the photoconductivity lifetime. On the other hand, the increase in photoconductivity lifetime observed for increasing Sb con-

tent correlates well with the decrease in defect density associated with Sb alloying in InAs nanowires.[41,42]

To investigate this correlation, high-resolution transmission electron microscope (TEM) images were carried out on all $InAs_{1-x}Sb_x$ and InAs nanowires to analyse their crystal structure as a function of Sb content, as shown in Figure 2(b-e). To describe the crystal structure in terms of both polytypism and stacking fault formation, we count the number of interfaces within the nanowire, i.e. the sum of zinc-blende/wurzite transitions, stacking faults and rotational twins. For the reference sample with InAs nanowires, wurtzite stacking was found to predominantly occur at the nanowire stem, with pure wurtzite segments of several tens of nanometres observed. To describe However, for the rest of the InAs nanowire, the defect density was extracted to be approximately 300 interfaces μm^{-1}. For increasing Sb content, a strong decrease in this defect density was observed, with defect densities of 220 interfaces μm^{-1}, 100 interfaces μm^{-1} and $\leq$ 1 interfaces μm^{-1} extracted for $InAs_{1-x}Sb_x$ NWs with 16%, 21% and 35% Sb content, respectively. Above 16% Sb content, the wurzite phase is completely suppressed and nanowires with 35% Sb content were determined to be an almost completely defect-free zinc-blende structures with only a few twin defects per micrometre.[41] Twin planes act to enhance charge carrier recombination, as they not only create unique surface electronic states that act as effect recombination centres, but also form type-II heterostructures and scatter free carriers to the trap-rich nanowire surface.[48,49] By reducing this defect density, Sb alloying reduces carrier trapping and recombination at defects, prolonging the carrier lifetime. As Sb content is increased, the photoconductivity lifetime also increases, with an increase of over a factor of 3 for $InAs_{0.65}Sb_{0.35}$ nanowires compared to InAs nanowires. Therefore, tuning the Sb content within III-V nanowires provides a means for tailoring photoconductivity lifetimes for nanowire-based devices.

Second, we investigate the effect of Sb incorporation on the electron mobility via both Raman and OPTP spectroscopy. These two non-contact techniques complement each other nicely as they both probe plasmon modes within the nanowire, with the width of the reso-

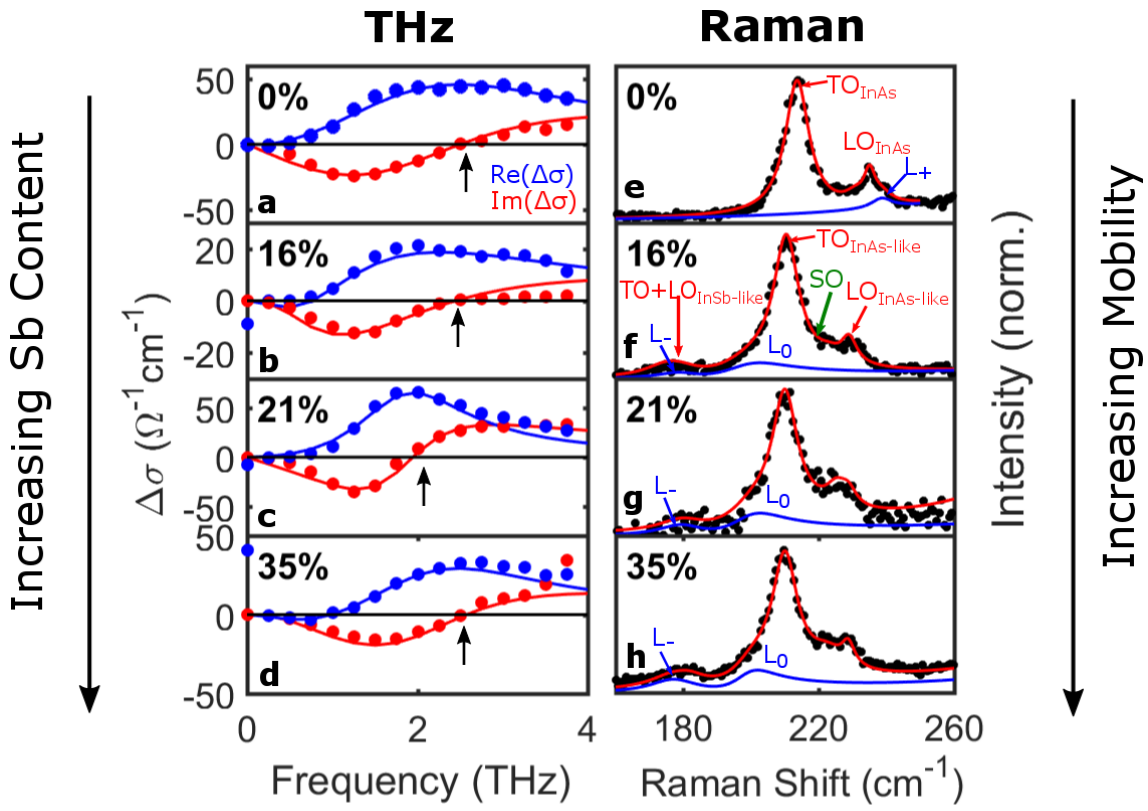

Figure 3: **Terahertz Photoconductivity Spectra:** Real (blue) and imaginary (red) part of the photoconductivity as a function of frequency for (a) the InAs and $InAs_{1-x}Sb_x$ nanowires with Sb concentrations of (b) 16%, (c) 21% and (d) 35% taken at 5 ps after photoexcitation at a fluence of 190 μ J cm^{-2} . Lorentzian fits to the data are shown by solid blue and red lines. **Raman Spectra:** Raman intensity as a function of Raman shift for (e) the InAs and $InAs_{1-x}Sb_x$ nanowires with Sb concentrations of (f) 16%, (g) 21% and (h) 35% . Spectra were taken for a single nanowire excited at 488nm with an average power of 250μ W.

nance mode directly related to the electron mobility and the position of the mode associated with the carrier concentration.[50] For both techniques, the electric field of the incident pulse forces charges to accumulate at the nanowire ends, creating an electric dipole with an associated depolarisation field that induces a plasmon mode within the nanowire. For terahertz spectroscopy, the plasmon mode is then observed directly by measuring the nanowire photoconductivity as a function of frequency. For Raman spectroscopy, on the other hand, the free electron oscillation couples with the longitudinal optical (LO) phonon mode within the nanowire and is observed by examination of the inelastically scattered light from the nanowires.[50–54] In-depth details of both spectroscopic techniques can be found in the Supporting Information.

Figure 3 shows THz photoconductivity and Raman spectra for $InAs_{1-x}Sb_x$ nanowires with Sb contents of 16%, 21% and 35% compared to InAs reference nanowires. For the THz photoconductivity spectra, the nanowires were again photoexcited at a wavelength of 800 nm and the time-resolved photoconductivity was measured as a function of frequency for a range of fluences between 0.49 and 190 $\mu\,J\,cm^{-2}$ and at a a time of 5 ps after photoexcitation. As can be seen from sample spectra taken at 190 $\mu\,J\,cm^{-2}$ (Figure 3(a-d)), a clear Lorentzian response in the photoconductivity is displayed, as previously seen for other III-V NWs.[25,55,56] As Sb content is increased, the width of this Lorentzian response narrows, indicating a reduction in the momentum scattering rate of electrons. However, for the $InAs_{0.65}Sb_{0.35}$ nanowires, the response broadens slightly, suggesting a saturation in the electron mobility at this level of Sb content. The position of the plasma frequency, depicted by black arrows in Figure 3(a-d), also red shifts with increasing Sb content, suggesting a slight increase in free carrier concentration.

For the Raman spectra, the nanowires were photoexcited with a continuous wave excitation laser at a centre wavelength of 488 nm with a laser power of 250 μW focused onto a single nanowire using a microscope objective and a numerical aperture of 0.75. The measurements were realized in back-scattering geometry with the nanowires suspended over a

trench, in order to enhance the response of the longitudinal optical phonon mode.[57] For the InAs nanowires, only TO and LO modes of the zinc-blende phase are present. For the $InAs_{1-x}Sb_x$ nanowires, on the other hand, the TO and LO modes follow the two-mode model for ternary alloys (see Supporting Information), displaying both a low (L_-) and high (L_+) frequency mode. In the presence of carriers, an additional LO phonon-plasmon coupled mode (LOPPCM) mode, L_0, is observed (solid blue lines in Figure 3(e-h)), which is confined in the frequency range between these two optical phonon branches. This LOPPCM mode exhibits plasmon-like character when it exhibits a frequency close to the plasma frequency, so its frequency position is directly related to the plasmon density (carrier concentration) and plasmon lifetime (carrier mobility).[58–61] Similar to the THz spectra, the width of these coupled modes can clearly be seen narrowing with increasing Sb content, again indicating a reduction in momentum scattering. The position of the mode also red-shifts slightly with frequency, indicating an increase in carrier concentration that is modulated by the modification in the Sb content in the alloy.

To extract both electron mobility and free carrier concentrations, the plasmon modes were fitted for both the THz and Raman spectra. Fluence-dependent THz photoconductivity spectra were fitted using a Lorentzian conductivity response for a free electron plasma that takes into account both photoexcited carriers and any extrinsic or dopant carriers (details found in the Supporting Information).[62] The solid lines in Figure 3(a-d) represent the fits from this model, which shows excellent agreement with the measured data for all samples. For the Raman spectra, the lineshape of the LOPPCM mode is evaluated using the dissipation fluctuation theorem, considering the standard dielectric theory in the formalism of Hon and Faust[58,59] (details in Supporting Information). The convolution of this fitted LOPPCM lineshape with the Lorentzian profile of the ternary TO and LO modes is depicted by the solid red lines in Figure 3(e-h), again showing excellent agreement to the measured data. The extracted electron mobilities and carrier concentrations for both spectroscopic techniques are presented in Figure 4. It can immediately be seen that the extracted values from both

techniques coincide well with each other, with values falling within error margins. This is an exciting result, as it is the first time that these two techniques have been directly compared and it highlights the accuracy of the two techniques.

For both techniques, a clear increase in electron mobility is observed with increasing Sb content: with $InAs_{0.65}Sb_{0.35}$ nanowires displaying electron mobilities of 7740±650 $cm^2V^{-1}s^{-1}$ and 8300±913 $cm^2V^{-1}s^{-1}$, over a factor of 3 higher than for the InAs nanowires at 2710±320 $cm^2V^{-1}s^{-1}$ and 3300±1900 $cm^2V^{-1}s^{-1}$. This increase in electron mobility is surprising, as alloy disorder scattering is expected to increase at higher Sb contents, degrading the electron mobility. However, it is important to note that for the reference InAs nanowires, transport occurs mainly at the surface due to Fermi level pinning, whereas for InAsSb nanowires bulk transport is expected to dominate, which could contribute to the enhancement of the electron mobility. However, when examining the free carrier concentrations as a function of Sb content, we find the values to be high for $InAs_{1-x}Sb_x$ nanowires, suggesting that transport at the donor-like surface states still plays a role.[25] It is important to note though that the free carrier concentration only slightly increases with increasing Sb content, as expected from spectra displayed in Figure 3. Therefore, it is not expected to have a significant contribution to the observed mobility enhancement. The solid line in Figure 4 displays calculated values for the inverse effective electron mass superimposed on top of the electron mobilities, demonstrating that this enhancement in electron mobility is primarily due to the reduction in effective electron mass with increasing Sb content. However, the enhancement of the electron mobility also coincides with the reduction in defect density offered by Sb incorporation. Yet, as defect scattering dominates at low temperatures, it is expected that the reduction in defect density offered by increased Sb content will play more of a significant role as temperature is decreased.

To further test the effect of the reduced defect density on the electron mobility, temperature-dependent terahertz and Raman measurements were carried out on the $InAs_{0.65}Sb_{0.35}$ nanowires and InAs reference nanowires. For both samples, terahertz photoconductivity spectra were

measured at 5 ps after the nanowires were photoexcited with 1.55 eV photons at a fluence of 244 μ J cm^{-2} for a range of temperatures between 10 and 300 K. Figure 5(a,b) shows sample spectra for the $InAs_{0.65}Sb_{0.35}$ nanowires taken at 300 K and 10 K respectively. From these spectra, a clear narrowing of the Lorentzian response is seen as the temperature is decreased, highlighting a decrease in momentum scattering and hence an increase in electron mobility. The plasma frequency is also red-shifted at 10 K, consistent with a reduction in free carrier density with decreasing temperature. One advantage of OPTP spectroscopy over Raman spectroscopy is that the extrinsic carrier concentration can also be extracted independently from the total free carrier concentration as a function of temperature to investigate the effect of dopant activation.[56] The extracted extrinsic carrier concentrations are plotted as a function of inverse temperature in the inset of Figure 5 for the $InAs_{0.65}Sb_{0.35}$ nanowires, where a clear activation energy is observed. By performing Arhenius analysis on the extracted values, an activation energy of 28 meV was determined, corresponding to an activation temperature of 216 K. As this activation energy is not seen for the reference InAs reference nanowires, it suggests that Sb alloying in InAs nanowires introduces a donor level within the nanowire. The result also highlights the use of terahertz spectroscopy for accurate doping characterisation within nanowires.

Alongside these measurements, Raman spectra were also measured for a range of temperatures between 14 K and 300 K at a power of 250 μW and sample spectra for temperatures of 14 K and 300 K are shown in Figure 5(d,e). A narrowing in the LOPPCM mode is again observed with decreasing temperature, indicative of a reduction in momentum scattering. The position of the LOPPCM mode also redshifts with decreasing temperature, as both the lattice constant and free carrier density decreases.[63] For both techniques, the electron mobilities were extracted for all temperatures for the $InAs_{0.65}Sb_{0.35}$ and InAs reference nanowires and are plotted in Figure 5(c). The two techniques display excellent agreement with each other, with extracted values for each technique falling within error of the other, again highlighting the accuracy of these non-contact methods, as well as the high growth

quality of the nanowires with single nanowire Raman measurements coinciding with ensemble THz measurements. For both samples, a clear increase in electron mobility is observed with decreasing temperature, displaying high mobilities of 16,000±210 $cm^2V^{-1}s^{-1}$ (THz) and 17,500±2450 $cm^2V^{-1}s^{-1}$ (Raman) at ∼10 K for the $InAs_{0.65}Sb_{0.35}$ nanowires compared to 6160±360 $cm^2V^{-1}s^{-1}$ (THz) and 5100±2200 $cm^2V^{-1}s^{-1}$ (Raman) at ∼10 K for the InAs reference nanowires. At low temperature (∼ 10 K), the electron mobility exhibits an enhancement close to a factor of 3 compared to the InAs reference nanowires. At temperatures below 100 K, a much sharper increase in electron mobility is observed for the $InAs_{0.65}Sb_{0.35}$ nanowires compared to the reference InAs nanowires. As defect scattering tends to dominate at low temperatures, the sharper gradient observed for the temperature-dependent mobility at low temperatures leads us to conclude that the large enhancement in the electron mobility is due to the reduction in defect density offered by Sb incorporation.

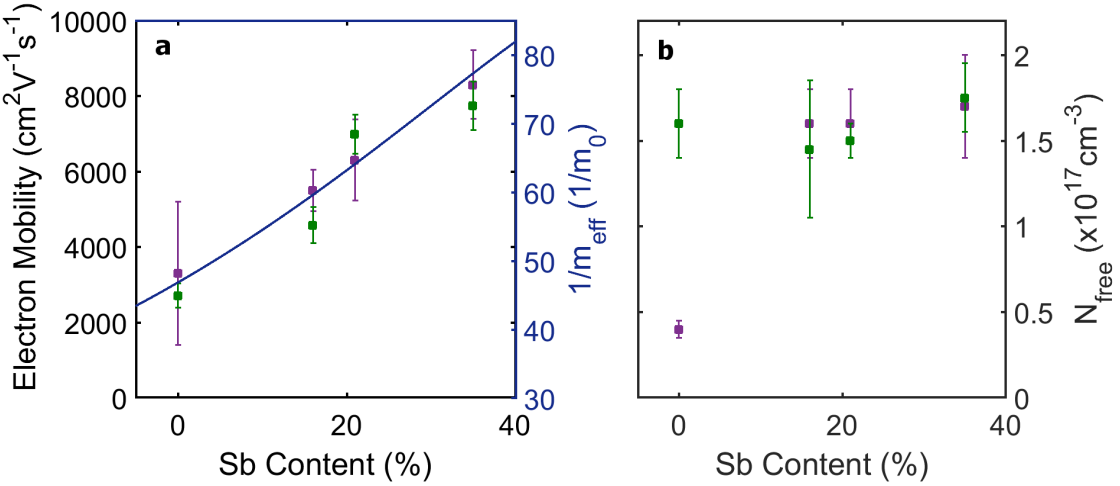

Figure 4: (a) Electron mobility values extracted from terahertz (green squares) and Raman (purple diamonds) measurements as a function of Sb content. Solid blue line represents the variation of the inverse effective electron mass as a functon of Sb content. (b) Free carrier concentrations extracted from terahertz (green) and Raman (purple) measurements.

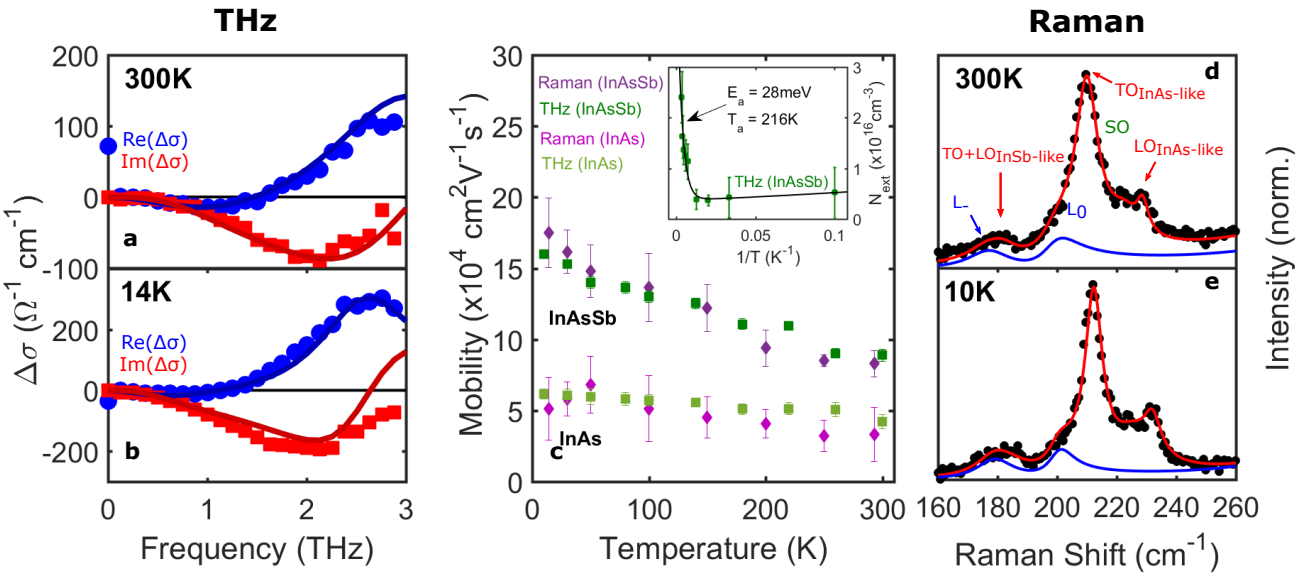

Figure 5: Terahertz photoconductivity spectra for the $InAs_{0.65}Sb_{0.35}$ nanowires taken 5 ps after photoexcitation at a fluence of 244 μ J cm^{-2} at temperatures of (a) 300 K and (b) 10 K. (c) Extracted electron mobilities from temperature-dependent terahertz (green squares) and Raman (purple diamonds) spectra as a function of temperature for both the $InAs_{0.65}Sb_{0.35}$ (dark colours) and InAs (light colours) nanowires. Inset: Extrinsic carrier concentrations for the $InAs_{0.65}Sb_{0.35}$ nanowires as a function of inverse temperature extracted from terahertz measurements. Raman spectra for the $InAs_{0.65}Sb_{0.35}$ nanowires excited at 488 nm at an average power of 250μW at temperatures of (d) 300 K and (e) 14 K.

Conclusions

In conclusion, Sb incorporation into InAs nanowires allows mid-infrared light emission to be tunded via optical bandgap engineering whilst enhancing their electrical performance. The lowest bandap acheived was 230 meV for nanowire with 35% Sb content, which corresponds to an emission wavelengh of 5.4 μm. From terahertz photoconductivity decay measurements, the photoconductivity lifetimes for the $InAs_{1-x}Sb_x$ nanowires were found to increase with Sb concentration, as a result of reduced crystal defects within the nanowire leading to a reduction in carrier trapping. A photoconductivity lifetime of 486 ± 30 ps was extracted for $InAs_{1-x}Sb_x$ nanowires with 35% Sb content, over a factor of 3 higher than the InAs nanowire sample. The electron mobility was also found to increase with increasing Sb content, with Raman and terahertz measurements both confirming a high electron mobility of $7170\pm650\,cm^2V^{-1}s^{-1}$ (THz) and $8300\pm913\,cm^2V^{-1}s^{-1}$ (Raman) for the $InAs_{0.65}Sb_{0.35}$ nanowires compared to $2710\pm320\,cm^2V^{-1}s^{-1}$ (THz) and $3300\pm1900\,cm^2V^{-1}s^{-1}$ (Raman) for the InAs reference nanowires. An enhancement by over a factor of 3 was observed for the $InAs_{0.65}Sb_{0.35}$ nanowires, with a high electron mobility between $16{,}000\pm210\,cm^2V^{-1}s^{-1}$ (THz) and $17{,}500\pm2450\,cm^2V^{-1}s^{-1}$ (Raman) extracted at 10 K. At low temperatures, a much sharper increase in the electron mobility was observed for the $InAs_{0.65}Sb_{0.35}$ nanowires compared to the InAs reference nanowires, indicating that the large mobility enhancement at low temperature is a direct result of the reduction in defect density offered by $InAs_{1-x}Sb_x$ nanowires. Thus,ternary $InAs_{1-x}Sb_x$ nanowires are prime candidates for use in both thermoelectric and optoelectronic devices with both high electrical conductivities and low thermal conductivities.

Acknowledgement

The authors thank the EPSRC (U.K.) and European Research Council (ERC) under the European Union's Horizon 2020 research and innovation programme (grant agreement 675867),

as well as the Swiss National Science Foundation via projects nr137648 and 156081

Supporting Information Available

The following can be found in the Supporting Information: nanowire growth details, experimental details for PL setup, OPTP and Raman setup, data analysis for OPTP and Raman spectroscopy, full temperature dependence of THz photoconductivity and Raman spectra.

References

(1) Lu, W.; Lieber, C. M. *39* **2006**, *21*, R387–R405.

(2) Im, J.-H.; Luo, J.; Franckevicius, M.; Pellet, N.; Gao, P.; Moeh, T.; Zakeeruddin, S. M.; Nazeeruddin, M. K.; Grätzel, M.; Park, N.-G. *Nano Letters* **2015**, *15*, 2120–2126.

(3) Yao, M.; Cong, S.; Arab, S.; Huang, N.; Povinelli, M. L.; Cronin, S. B.; Dapkus, P. D.; Zhou, C. *Nano Letters* **2015**, *15*, 7217–7224.

(4) Han, N.; Yang, Z.-x.; Wang, F.; Dong, G.; Yip, S.; Liang, X.; Hung, T. F.; Chen, Y.; Ho, J. C. *ACS Applied Materials and InterfacesApplied Materials & Interfaces* **2015**, *7*, 20454–20459.

(5) Krogstrup, P.; Jørgensen, H. I.; Heiss, M.; Holm, J. V.; Aagesen, M.; Nygard, J.; Fontcuberta, A. *Nature Photonics* **2013**, *7*, 1–19.

(6) Dong, Y.; Tian, B.; Kempa, T. J.; Lieber, C. M.; Dong, Y.; Tian, B.; Kempa, T. J.; Lieber, C. M. *Nano Letters* **2009**, *9*, 2183–2187.

(7) Morkötter, S.; Jeon, N.; Rudolph, D.; Loitsch, B.; Spirkoska, D.; Hoffmann, E.; Döblinger, M.; Matich, S.; Finley, J. J.; Lauhon, L. J.; Abstreiter, G.; Koblmüller, G. *Nano Letters* **2015**, *15*, 3295–3302.

(8) Tomioka, K.; Yoshimura, M.; Fukui, T. *Nature* **2012**, *488*, 0–4.

(9) Svensson, J.; Dey, A. W.; Jacobsson, D.; Wernersson, L. E. *Nano Letters* **2015**, *15*, 7898–7904.

(10) Lee, B.-H.; Hur, J.; Kang, M.-H.; Bang, T.; Ahn, D.-C.; Lee, D.; Kim, K.-h.; Choi, Y.-k. *Nano Letters* **2016**, *16*, 1840–1847.

(11) Zhao, Q. T.; Hartmann, J. M.; Mantl, S. *IEEE Electron Device Letters* **2011**, *32*, 1480–1482.

(12) Saxena, D.; Jiang, N.; Yuan, X.; Mokkapati, S.; Guo, Y.; Tan, H. H.; Jagadish, C. *Nano Letters* **2016**, *16*, 5080–5086.

(13) Röder, R.; Sidiropoulos, T. P. H.; Tessarek, C.; Christiansen, S.; Oulton, R. F.; Ronning, C. *Nano Letters* **2015**, *15*, 4637–4643.

(14) Mayer, B.; Janker, L.; Loitsch, B.; Treu, J.; Kostenbader, T.; Lichtmannecker, S.; Reichert, T.; Morko, S.; Kaniber, M.; Abstreiter, G.; Gies, C.; Koblmu, G.; Finley, J. J. *Nano Letters* **2016**, *16*, 152–156.

(15) Burgess, T.; Saxena, D.; Mokkapati, S.; Li, Z.; Hall, C. R.; Davis, J. A.; Wang, Y.; Smith, L. M.; Fu, L.; Caroff, P.; Tan, H. H.; Jagadish, C. *Nature Communications* **2016**, *7*, 1–7.

(16) Piccione, B.; Cho, C.-h.; Vugt, L. K. V.; Agarwal, R. *Nature Nanotechnology* **2012**, *7*, 640–645.

(17) Romeo, L.; Coquillat, D.; Husanu, E.; Ercolani, D.; Tredicucci, A.; Beltram, F.; Sorba, L.; Knap, W.; Vitiello, M. S. *Applied Physics Letters* **2014**, *105*, 231112.

(18) Vitiello, M. S.; Coquillat, D.; Viti, L.; Ercolani, D.; Teppe, F.; Pitanti, A.; Beltram, F.; Sorba, L.; Knap, W.; Tredicucci, A. *Nano Letters* **2012**, *12*, 96–101.

(19) Peng, K.; Parkinson, P.; Boland, J. L.; Gao, Q.; Wenas, Y. C.; Davies, C. L.; Li, Z.; Fu, L.; Johnston, M. B.; Tan, H. H. *Nano Letters* **2016**, *16*, 4925–4931.

(20) Peng, K.; Parkinson, P.; Gao, Q.; Boland, J. L.; Li, Z.; Wang, F.; Mokkapati, S.; Fu, L.; Johnston, M. B.; Tan, H. H. *Nanotechnology* **2017**, *28*, 125202.

(21) Plissard, S.; Dick, K. A.; Wallart, X.; Caroff, P. *Applied Physics Letters* **2010**, *96*, 1219011–1219013.

(22) Dheeraj, D. L.; Patriarche, G.; Zhou, H.; Hoang, T. B.; Moses, A. F.; Grønsberg, S.; Van Helvoort, A. T. J.; Fimland, B. O.; Weman, H. *Nano Letters* **2008**, *8*, 4459–4463.

(23) Conesa-Boj, S.; Kriegner, D.; Han, X.-L.; Plissard, S.; Wallart, X.; Stangl, J.; Fontcuberta i Morral, A.; Caroff, P. *Nano Letters* **2014**, *14*, 326–332, PMID: 24329502.

(24) Dayeh, S. A.; Aplin, D. P. R.; Zhou, X.; Yu, P. K. L.; Yu, E. T.; Wang, D. *Small* **2007**, *3*, 326–332.

(25) Joyce, H. J.; Docherty, C. J.; Gao, Q.; Tan, H. H.; Jagadish, C.; Lloyd-hughes, J.; Herz, L. M. *Nanotechnology* **2013**, *24*, 214006.

(26) Mourik, V.; Zuo, K.; Frolov, S. M.; Plissard, S. R.; Bakkers, E. P. A. M. *Science* **2012**, *336*, 1003–1007.

(27) Plissard, S.; van Weperen, I.; Car, D.; Verheijen, M.; Immink, G. W. G.; Kammhuber, J.; Cornelissen, L. J.; Szombati, D. B.; Geresdi, A.; Frolov, S. M.; Kouwenhoven, L. P.; Bakkers, E. P. A. M. *Nature Nanotechnology* **2013**, *8*, 859–864.

(28) Mattias Borg, B.; Wernersson, L.-E. *Nanotechnology* **2013**, *24*, 202001.

(29) Svensson, J.; Anttu, N.; Vainorius, N.; Borg, B. M. *Nano Letters* **2013**, *13*, 1380–1385.

(30) Vurgaftman, I.; Meyer, J. R.; Ram-Mohan, L. R. *Journal of Applied Physics* **2001**, *89*, 5815–5875.

(31) Bowers, R.; Bauerle, J. E.; Cornish, A. J. *Journal of Applied Physics* **1959**, *930*, 930–934.

(32) Seol, J. H.; Moore, A. L.; Saha, S. K.; Zhou, F.; Shi, L.; Ye, Q. L.; Scheffler, R.; Mingo, N.; Yamada, T. *Journal of applied physics* **2007**, *101*, 023706.

(33) Tian, Y.; Sakr, M. R.; Kinder, J. M.; Liang, D.; MacDonald, M. J.; Qiu, R. L.; Gao, H.-J.; Gao, X. P. *Nano letters* **2012**, *12*, 6492–6497.

(34) Zhou, F.; Moore, A. L.; Bolinsson, J.; Persson, A.; Fröberg, L.; Pettes, M. T.; Kong, H.; Rabenberg, L.; Caroff, P.; Stewart, D. A. *Physical Review B* **2011**, *83*, 205416.

(35) Zhou, F.; Seol, J.; Moore, A.; Shi, L.; Ye, Q.; Scheffler, R. *Journal of Physics: Condensed Matter* **2006**, *18*, 9651.

(36) Yazji, S.; Swinkels, M. Y.; De Luca, M.; Hoffmann, E.; Ercolani, D.; Roddaro, S.; Abstreiter, G.; Sorba, L.; Bakkers, E. P.; Zardo, I. *Semiconductor Science and Technology* **2016**, *31*, 064001.

(37) der Gl,; van Woerkom, D. J.; van Weperen, I.; Car, D.; Plissard, S. R.; Bakkers, E. P. A. M.; Kouwenhoven, L. P. *Nanotechnology* **2015**, *26*, 215202.

(38) Anyebe, E. A.; Rajpalke, M. K.; Veal, T. D.; Jin, C. J.; Wang, Z. M.; Zhuang, Q. D. *Nano Research* **2015**, *8*, 1309–1319.

(39) Zhuang, Q. D.; Anyebe, E. A.; Chen, R.; Liu, H.; Sanchez, A. M.; Rajpalke, M. K.; Veal, T. D.; Wang, Z. M.; Huang, Y. Z.; Sun, H. D. *Nano Letters* **2015**, *15*, 1109–1116.

(40) Farrell, A. C.; Lee, W.-j.; Senanayake, P.; Haddad, M. A.; Prikhodko, S. V.; Hu, D. L. *Nano Letters* **2015**, *15*, 6614–6619.

(41) Potts, H.; Friedl, M.; Amaduzzi, F.; Tang, K.; Tütüncüoglu, G.; Matteini, F.; Alarcon Lladó, E.; McIntyre, P. C.; Fontcuberta i Morral, A. *Nano Letters* **2016**, *16*, 637–643.

(42) Sourribes, M. J. L.; Isakov, I.; Pan, M.; Liu, H.; Warburton, P. A. *Nano Letters* **2014**, *14*, 1643–1650.

(43) Fang, Z. M.; Ma, K. Y.; Jaw, D. H.; Cohen, R. M.; Stringfellow, G. B. *Applied Physics Letters* **1990**, *67*.

(44) Van Vechten, J. A.; Bergstresser, T. K. *Phys. Rev. B* **1970**, *1*, 3351–3358.

(45) Potts, H.; Friedl, M.; Amaduzzi, F.; Tang, K.; Matteini, F.; Llado, E. A.; Mcintyre, P. C.; Fontcuberta, A. *Nano Letters* **2016**, *16*, 637–643.

(46) Thelander, C.; Caroff, P.; Plissard, S.; Dey, A. W.; Dick, K. A. *Nano Lett.* **2011**, *11*, 2424–2429.

(47) Joyce, H. J.; Boland, J. L.; Davies, C. L.; Baig, S. A.; Johnston, M. B. *Semiconductor Science and Technology* **2016**, *31*, 1–21.

(48) Brown, E.; Sheng, C.; Shimamura, K.; Shimojo, F.; Nakano, A. *Journal of Applied Physics* **2015**, *117*.

(49) Parkinson, P.; Joyce, H. J.; Gao, Q.; Tan, H. H.; Zhang, X.; Zou, J.; Jagadish, C.; Herz, L. M.; Johnston, M. B. *Nano Letters* **2009**, *9*, 3349–3353.

(50) Takeuchi, H.; Sumioka, T.; Nakayama, M. *IEEE Transactions on Terahertz Science and Technology* **2017**, *7*, 124–130.

(51) Nowak, U.; Richter, W.; Sachs, G. *physica status solidi (b)* **1981**, *108*, 131–143.

(52) Ketterer, B.; Arbiol, J.; Fontcuberta i Morral, A. *Phys. Rev. B* **2011**, *83*, 245327.

(53) Cuscó, R.; Artús, L.; Hernández, S.; Ibáñez, J.; Hopkinson, M. *Physical Review B* **2001**, *65*, 035210.

(54) Jeganathan, K.; Debnath, R. K.; Meijers, R.; Stoica, T.; Calarco, R.; Grützmacher, D.; Lüth, H. *Journal of Applied Physics* **2009**, *105*.

(55) Boland, J. L.; Casadei, A.; Matteini, F.; Davies, C. L.; Jabeen, F.; Joyce, H. J.; Herz, L. M.; Fontcuberta, A.; Johnston, M. B. *ACS Nano* **2016**, *10*, 4219–4227.

(56) Gül, Ö.; Van Woerkom, D. J.; van Weperen, I.; Car, D.; Plissard, S. R.; Bakkers, E. P.; Kouwenhoven, L. P. *Nanotechnology* **2015**, *26*, 215202.

(57) Amaduzzi, F.; Alarcón-Lladó, E.; Hautmann, H.; Tanta, R.; Matteini, F.; Tütüncüolu, G.; Vosch, T.; Nygård, J.; Jespersen, T.; Uccelli, E. *Journal of Physics D: Applied Physics* **2016**, *49*, 095103.

(58) Hon, D. T.; Faust, W. L.; Spitzer, W. G.; Williams, P. F. *Phys. Rev. Lett.* **1970**, *25*, 1184–1187.

(59) Hon, D. T.; Faust, W. L. *Applied Physics* **1968**, *1*, 241–256.

(60) Buchner, S.; Burstein, E. *Physical Review Letters* **1974**, *33*, 908–911.

(61) Li, Y. B.; Ferguson, I. T.; Stradling, R. A.; Zallen, R. *Semiconductor Science and Technology* **1992**, *7*, 1149.

(62) Boland, J. L.; Conesa-Boj, S.; Parkinson, P.; Tütüncüoglu, G.; Matteini, F.; Rüffer, D.; Casadei, A.; Amaduzzi, F.; Jabeen, F.; Davies, C. L.; Joyce, H. J.; Herz, L. M.; Fontcuberta i Morral, A.; Johnston, M. B. *Nano Letters* **2015**, *15*, 1336–1342.

(63) Hart, T.; Aggarwal, R.; Lax, B. *Physical Review B* **1970**, *1*, 638–642.